Shifts due to quantum-mechanical interference from distant neighboring resonances for saturated fluorescence spectroscopy of the $2\,^3S$ to $2\,^3P$ intervals of helium

A. Marsman, E. A. Hessels,* and M. Horbatsch
Department of Physics and Astronomy, York University, Toronto, Ontario, Canada M3J 1P3
(Received 16 February 2014; published 3 April 2014)

Quantum-mechanical interference with distant neighboring resonances is found to cause shifts for precision saturated fluorescence spectroscopy of the atomic helium $2\,^3S$-to-$2\,^3P$ transitions. The shifts are significant (larger than the experimental uncertainties for measurements of the intervals) despite the fact that the neighboring resonances are separated from the measured resonances by 1400 and 20 000 natural widths. The shifts depend strongly on experimental parameters such as the angular position of the fluorescence detector, the intensity and size of laser beams, and the properties of the atomic beam. These shifts must be considered for the ongoing program of determining the fine-structure constant from the helium $2\,^3P$ fine structure.

DOI: 10.1103/PhysRevA.89.043403 PACS number(s): 32.70.Jz, 32.80.−t, 33.40.+f

I. INTRODUCTION

In previous work [1,2], we have demonstrated that a resonance can be shifted by quantum-mechanical interference with a distant neighboring resonance for a simple three- or four-level atom interacting with a constant-amplitude sinusoidal driving field. Similar shifts in more complicated systems, such as the helium $n = 2$ triplet states considered here, depend critically on the experimental technique used to determine the intervals. An evaluation [3] of interference effects for microwave transitions between $2\,^3P$ states (such as in the precision measurements of Refs. [4,5]) reveals small shifts, with the shifts being even smaller for measurements that use the Ramsey technique of separated oscillatory fields (such as the precision measurement of Ref. [6]). An evaluation [7] of interference effects for laser $2\,^3S$-to-$2\,^3P$ transitions (such as the precision measurement of Ref. [8]), on the other hand, reveals shifts larger than the experimental uncertainty. In that work, the laser transitions are detected by the transfer of population between metastable $2\,^3S$ states. The effect of interference can be seen more directly when the resonances are not distant, as has been shown recently for the overlapping hyperfine components for lithium D lines [9].

Here we calculate interference shifts for saturated fluorescence spectroscopy in an atomic beam of metastable helium atoms (similar to the experimental work in Refs. [10,11]), and find that quite substantial shifts occur for this measurement technique. Saturated fluorescence uses two counterpropagating laser beams, each with intensity above the saturated intensity for the transition, and a reduction in fluorescence is observed when the laser frequency is tuned onto resonance. This reduction results [12] from the fact that the two lasers cause atoms in separated velocity classes (Doppler shifts) to fluoresce when the laser is tuned away from resonance, but both lasers address the same velocity class when the laser is on resonance. We consider the effect of neighboring resonances on saturated fluorescence for the $2\,^3S_1$-to-$2\,^3P_1$ and $2\,^3S_1$-to-$2\,^3P_0$ transitions (Fig. 1). The $2\,^3P_1$-to-$2\,^3P_0$ fine-structure interval, which can be used to determine the fine-structure constant α, can be obtained from the difference between the two resonance centers.

The program for determining α from the $2\,^3P$ intervals has been ongoing for almost 50 years [13], with theoretical [14–16] and experimental [4–6,8,10,17–19] contributions continuing, and a determination of α from these intervals to better than a part per billion may soon be possible.

II. SATURATED FLUORESCENCE LINE SHAPE

A. Density-matrix equations

As in the saturated fluorescence measurement of Refs. [10,11], we consider two counterpropagating laser beams (along $\pm\hat{y}$), with both beams having the same waist size, frequency ($\omega/2\pi$), peak intensity (I_0), and linear polarization ($\hat{z}$). The calculation uses $\hat{z}$ as the quantization axis, consistent with the energy levels of Fig. 1. In order to analyze saturated fluorescence spectroscopy, each Doppler group (with atomic velocity component v_y) within the atomic beam must be considered separately, with the full signal resulting from the average of all Doppler groups present. An atom which has a velocity component v_y sees equal and opposite Doppler shifts $\pm\Delta\omega_D = \pm 2\pi\,\Delta f_D = \pm\omega v_y/c$ for the two laser beams. The two laser beams form a standing wave with the total $\vec{E} = \hat{z}E_S(t)\cos(\omega t - \bar{\phi})$ seen by the moving atom as it passes through the laser beams, where

$$E_S(t) = 2E_0\cos(\Delta\omega_D t + \Delta\phi/2)e^{-2(t-t_L)^2/T_L^2}. \qquad (1)$$

Here, $E_0 = \sqrt{\frac{2I_0}{\epsilon_0 c}}$, $\bar{\phi}$ and $\Delta\phi$ are the average and difference of the phases of the two laser beams, t_L is the time at which the atom passes through the center of the laser beam, and T_L determines the interaction time between the atom and the laser, and is based on the speed of the atom and the waist of the laser beam. We ignore the nonresonant $e^{-i\omega t}$ term and use the rotating-wave approximation. In this approximation, using the notation $|g_\mu\rangle = |2^3S_1 m_J = \mu\rangle$ and $|e_{jm}\rangle = |2^3P_j m_J = m\rangle$ of Fig. 1, we obtain the density-matrix

*hessels@yorku.ca

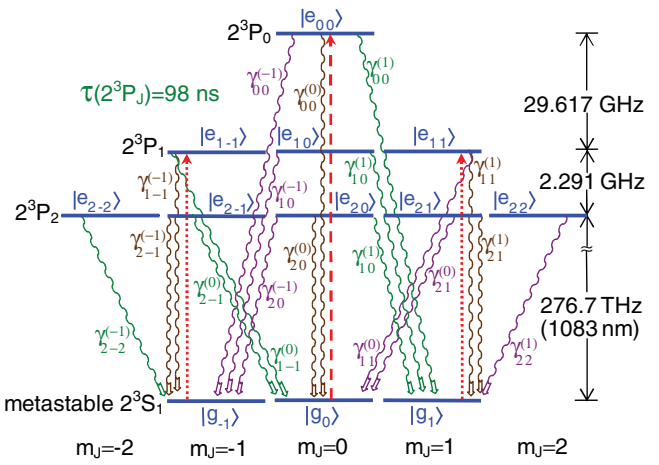

FIG. 1. (Color online) The $n = 2$ triplet energy levels of helium. The metastable states are labeled $|g_\mu\rangle$ and the $2^3P_J(m_J = m)$ states are labeled $|e_{Jm}\rangle$. The transitions being considered are shown as dashed and dotted red arrows, and all radiative decay paths are shown, with $\gamma^{(\mu)}_{Jm}$ being the decay rate from $|e_{Jm}\rangle$ to $|g_\mu\rangle$. Interference between decays that have the same Δm_J (the same color in the figure) and end in the same $|g_\mu\rangle$ state leads to the shifts discussed in this work.

equations [1,2,7,20]

$$\dot{\rho}_{g_\mu g_{\mu'}} = \sum_{j,m,j',m'} \gamma^{\mu' j' m'}_{\mu j m} \rho_{e_{jm} e_{j'm'}} + i \sum_{j,m} \frac{\Omega_{\mu' jm} \rho_{g_\mu e_{jm}} - \Omega^*_{\mu jm} \rho_{e_{jm} g_{\mu'}}}{2},$$

$$\dot{\rho}_{e_{jm} e_{j'm'}} = \frac{\omega_j - \omega_{j'}}{i} \rho_{e_{jm} e_{j'm'}} + i \sum_{\mu} \frac{\Omega^*_{\mu j'm'} \rho_{e_{jm} g_\mu} - \Omega_{\mu jm} \rho_{g_\mu e_{j'm'}}}{2} - \sum_{\mu, j''} \frac{\gamma^{\mu j'' m}_{\mu j m} \rho_{e_{j''m} e_{j'm'}} + \gamma^{\mu j'' m'}_{\mu j' m'} \rho_{e_{jm} e_{j''m'}}}{2},$$

$$\dot{\rho}_{g_\mu e_{jm}} = \frac{\omega - \omega_j}{i} \rho_{g_\mu e_{jm}} - \sum_{\mu', j', m'} \frac{\gamma^{\mu' j' m'}_{\mu' jm}}{2} \rho_{g_\mu e_{j'm'}} + \frac{i}{2} \sum_{\mu'} \Omega^*_{\mu' jm} \rho_{g_\mu g_{\mu'}} - \frac{i}{2} \sum_{j', m'} \Omega^*_{\mu j' m'} \rho_{e_{j'm'} e_{jm}}, \quad (2)$$

where

$$\Omega_{\mu jm} = \Omega_{\mu jm}(t) = \frac{e E_S(t)}{\hbar} \langle g_\mu | z | e_{jm} \rangle, \quad (3a)$$

$$\gamma^{\mu' j' m'}_{\mu j m} = \frac{e^2 \overline{\omega}^3}{3\pi \epsilon_0 \hbar c^3} \langle g_\mu | \vec{r} \, | e_{jm} \rangle \langle e_{j'm'} | \vec{r} \, | g_{\mu'} \rangle, \quad (3b)$$

and the $q = 0, \pm 1$ components of $\langle g_\mu | r_q | e_{jm} \rangle$ are

$$\langle g_\mu | r_q | e_{jm} \rangle = \frac{(-1)^{1-\mu}}{\sqrt{3}/\sqrt{2j+1}} \begin{pmatrix} 1 & 1 & j \\ -\mu & q & m \end{pmatrix} 4.385 a_0. \quad (4)$$

The $\gamma^{\mu' j' m'}_{\mu j m}$ terms in Eq. (2) include the partial rates $\gamma^{(\mu)}_{jm} = \gamma^{\mu j m}_{\mu j m}$ for radiative decay from $|e_{jm}\rangle$ to $|g_\mu\rangle$ (as shown in Fig. 1), and the total decay rate $1/\tau = \gamma = \sum_\mu \gamma^{(\mu)}_{jm}$. The latter has the same value for all $|e_{jm}\rangle$ since the 2^3S_1-to-2^3P_j energy interval $\hbar\omega_j = h f_j$ is approximated by its average value $\hbar\overline{\omega}$ in Eq. (3b). The off-diagonal $\gamma^{\mu' j' m'}_{\mu j m}$ terms represent interferences between the partial rates, and these interferences lead to the shifts calculated in this work. Often calculations using density-matrix equations neglect these terms and therefore do not include interference effects.

B. Efficient solution method

The 144 coupled equations represented in Eq. (2) are complete but challenging to solve numerically due to the fast oscillations caused by the large $\omega_j - \omega_{j'}$ and $\omega - \omega_j$ terms. If we are considering a laser that is nearly resonant with the $|g_\mu\rangle$-to-$|e_{Jm}\rangle$ transition (i.e., in resonance with the $j = J$ state), the other states ($\rho_{e_{j'm} e_{j'm}}$, with $j' \neq J$) obtain very little population. Similarly to Refs. [1,2], we note that all $\omega_{Jj'} = \omega_J - \omega_{j'}$ (which are $\gtrsim 2\pi$ times the He 2^3P fine-structure splittings of Fig. 1) are more than 1000 times larger than the other frequency scales in Eq. (2) ($\gamma^{\mu' j' m'}_{\mu j m}$, $1/T_L$, $\Omega_{\mu jm}$, and $\Delta = 2\pi\Delta f = \omega - \omega_J$), all of which are $\lesssim 1/\tau$. Introducing a small scale parameter η which is the ratio of these two frequency scales allows an expansion of Eq. (2) in η. As in Refs. [1,2], the η^2 terms (e.g., $\rho_{e_{j'm} e_{j'm}}$) can be ignored and the density-matrix elements of order η (e.g., $\rho_{e_{Jm} e_{j'm}}$ and $\rho_{e_{j'm} g_\mu}$) can be eliminated to give modified equations for the dominant density-matrix elements that are complete to order η:

$$\dot{\rho}_{g_\mu g_{\mu'}} = i(\epsilon_{\mu'} - \epsilon_\mu) \rho_{g_\mu g_{\mu'}} + \frac{i}{2} \sum_m [\Omega_{\mu' Jm} \rho_{g_\mu e_{Jm}} - \Omega^*_{\mu Jm} \rho_{e_{Jm} g_{\mu'}}] + \sum_{m, \mu''} \left[\zeta^{Jm}_{\mu \mu' \mu''} \rho_{g_{\mu''} e_{Jm}} + \left(\zeta^{Jm}_{\mu' \mu \mu''} \right)^* \rho_{e_{Jm} g_{\mu''}} \right] + \sum_{m, m'} \gamma^{\mu' Jm'}_{\mu Jm} \rho_{e_{Jm} e_{Jm'}},$$

$$\dot{\rho}_{e_{Jm} e_{Jm'}} = -\gamma \rho_{e_{Jm} e_{Jm'}} - \frac{i}{2} \sum_\mu \left[\Omega_{\mu Jm} \rho_{g_\mu e_{Jm'}} - \Omega^*_{\mu Jm'} \rho_{e_{Jm} g_\mu} \right],$$

$$\dot{\rho}_{g_\mu e_{Jm}} = \sum_{\mu'} \frac{i \Omega^*_{\mu' Jm}}{2} \rho_{g_\mu g_{\mu'}} - \sum_{m'} \frac{i \Omega^*_{\mu Jm'}}{2} \rho_{e_{Jm'} e_{Jm}} - \sum_{\mu'} \frac{\gamma^{\mu' Jm}_{\mu' Jm}}{2} \rho_{g_\mu e_{Jm}} - i(\omega - \omega_J + \epsilon_\mu) \rho_{g_\mu e_{Jm}}. \quad (5)$$

Here,

$$\epsilon_\mu = \sum_{j' \neq J, m'} \frac{|\Omega_{\mu j' m'}|^2}{4\omega_{Jj'}} \quad \text{and} \quad \zeta^{Jm}_{\mu \mu' \mu''} = \sum_{j \neq J, m'} \frac{\Omega_{\mu'' jm'} \gamma^{\mu' Jm}_{\mu jm'}}{2\omega_{Jj}} \quad (6)$$

result from perturbations due to the distant $|e_{j'm'}\rangle$ states and are the only terms of order η in Eq. (5). The ϵ_μ terms represent the ac Stark shift of the $|g_\mu\rangle$ state. The ζ terms lead to the

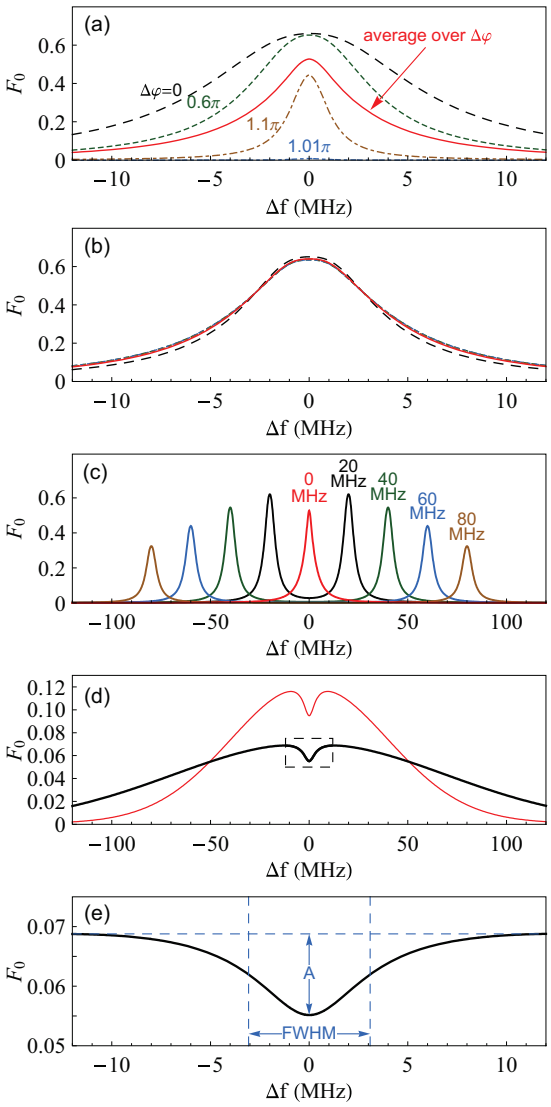

FIG. 2. (Color online) The fluorescence signals F_0 as a function of detuning Δf from the $2\,^3S_1$-to-$2\,^3P_1$ resonance. Individual Doppler groups Δf_D, (a)–(c), give resonances at $\Delta f = \pm\Delta f_D$. For small Δf_D, F_0 depends on the relative phase, as shown for four values of $\Delta\phi$ in (a). At larger Δf_D, the dependence is reduced substantially, as shown for the same values of $\Delta\phi$ for $\Delta f_D = 0.4$ MHz in (b). The solid curves represent averages over $\Delta\phi$. The average of F_0 over all Doppler groups leads to the saturated fluorescence dip, as shown in (d) for $\Delta f_D^{\rm HWHM} = 45$ MHz (thin red line) and 80 MHz (thick line). An expanded view of the saturated fluorescence dip within the dashed area in (d) is shown in (e), along with the amplitude (A) and full width at half maximum (FWHM) of the dip.

interference shifts being discussed in this work and these terms are the generalization of the $\Omega_2' - \Omega_2$ terms in Eq. (10) in Ref. [1] (which treats the three-level system) and of the $\Omega_{2\pm}' - \Omega_2$ and $\Omega_2'' - \Omega_2$ terms in Eq. (3) in Ref. [2] (which treats the four-level problem). Equation (5) gives 16, 36, or 64 equations (for $J = 0$, 1, or 2, respectively), and these equations lack the fast oscillations found in Eq. (2), and thus require a factor of η (three orders of magnitude) fewer time steps for the numerical integration. The results of these integrations agree with those from Eq. (2) to order η^2 (i.e., to better than a part per million).

C. Fluorescence

The fluorescence emitted by the laser-excited atoms can be obtained from the γ terms in the $\dot\rho_{e_{jm}e_{j'm'}}$ equation of Eq. (2). The fluorescence has three components F_q ($q = 0, \pm1$) which represents fluorescence for $\Delta m_J = 0, \pm1$ decays from the $2\,^3P_J$ state to the $2\,^3S_1$ state. The fluorescence F_q is given by

$$F_q = \int_{t_i}^{t_f} dt \sum_{\mu,j,m,j'} \delta_\mu^{m+q} \gamma_{\mu jm}^{\mu j'm} \frac{\rho_{e_{j'm}e_{jm}} + \rho_{e_{jm}e_{j'm}}}{2}. \quad (7)$$

Here the Kronecker delta selects the component of the fluorescence based on the m_J quantum numbers of the upper and lower states, and the integration is over the time that the moving atom spends in the laser beam.

Using techniques similar to those from the previous section, one can find an expression for the terms in Eq. (7) that is correct to first order in η:

$$F_q = \int_{t_i}^{t_f} dt \sum_{\mu,m} \delta_\mu^{m+q} \Big\{ \gamma_{\mu Jm}^{\mu Jm} \rho_{e_{Jm}e_{Jm}} + \sum_{\mu'} [\zeta_{\mu\mu\mu'}^{Jm} \rho_{g_{\mu'}e_{Jm}} + (\zeta_{\mu\mu\mu'}^{Jm})^* \rho_{e_{Jm}g_{\mu'}}] \Big\}. \quad (8)$$

For each Doppler group, the solution to Eq. (5) can be used to obtain F_q from Eq. (8). Equal initial populations are assumed for the three metastable states $|g_\mu\rangle$.

The solutions F_0 for the $J = 1$ case (the $2\,^3S_1$-to-$2\,^3P_1$ transition using $I_0 = 2$ mW/cm^2 and $T = 1$ μs) are shown in Fig. 2(a) for the $\Delta f_D = 0$ ($v_y = 0$) Doppler group. Note from the figure that the fluorescence depends strongly on the relative phase $\Delta\phi$ between the two laser fields. As shown in Fig. 2(b), at larger Δf_D (larger v_y), the dependence on $\Delta\phi$ becomes small because the atoms sample all relative phases while passing through the standing wave. Since, in practice, this relative phase would vary, the average over all values of $\Delta\phi$ is used, as shown by the solid lines in Figs. 2(a)–2(c). Figure 2(d) shows the fluorescence for a weighted average of the Doppler groups included. Here we have assumed a Gaussian distribution for v_y and therefore a Gaussian distribution of Doppler groups (with half width at half maximum of $\Delta f_D^{\rm HWHM}$). The reduced signal near resonance is the saturated fluorescence dip, and is shown in an expanded view in Fig. 2(e).

The amplitude and width of the dip [Fig. 2(e)] as a function of I_0 are shown in Fig. 3 for three values of T_L. For the dip to have a substantial amplitude [Fig. 3(a)], it is necessary that the laser intensity be above the saturation intensity for the transition, and at these intensities, the width [Fig. 3(b)] is broadened relative to the 1.6-MHz natural width for the transition. For precision measurements of the saturated fluorescence dip, there is a trade-off between dip amplitude and dip width, with intensities that lead to widths ranging from 5 to 15 MHz being reasonable for the measurements.

III. ac STARK SHIFT

Before considering the interference shifts due to off-diagonal $\gamma_{\mu jm}^{\mu' j'm'}$, we analyze the ac Stark shifts. To isolate these shifts, we solve Eqs. (5) and (8) while temporarily setting the off-diagonal $\gamma_{\mu jm}^{\mu' j'm'}$ terms to zero to artificially

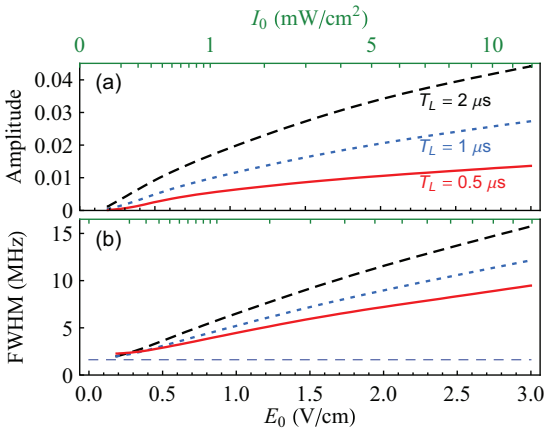

FIG. 3. (Color online) The amplitude and width of the $2\,^3S_1$-to-$2\,^3P_1$ saturated fluorescence dip [Fig. 2(e)] as a function of intensity I_0 for three choices of interaction time T_L, as labeled in (a). The width of the dips is significantly broader than the natural width [thin dashed line in (b)] for intensities that lead to dips of substantial amplitude.

suppress the interference shifts. The ac Stark shift results from ϵ_μ of Eq. (6), and it causes all of the resonances of Figs. 2(a)–2(c) (for all Doppler groups) to shift to the left. The magnitude of these shifts is complicated by the fact that the ac electric-field amplitude [Eq. (1)] depends on t, Δf_D, and $\Delta\phi$. The t dependence requires an integration over time of Eqs. (5) and (8) to determine the shifted line shape. This line shape is then averaged over $\Delta\phi$. For small values of Δf_D, this average is complicated by the fact that constructive interference leads to both a large resonance [$\Delta\phi = 0$ of Fig. 2(a)] and a large shift, whereas destructive interference [$\Delta\phi \approx \pi$ of Fig. 2(a)] leads to no signal and no shift. Finally, the shift is complicated by the Δf_D dependence, in that a leftward shift of the peak from small Δf_D contributions [such as the $\Delta f_D = 0$ case in Fig. 2(c)] causes the dip of Fig. 2(d) to move to the right. However, since the higher Δf_D contributions [such as the $\Delta f_D = 20$ MHz case in Fig. 2(c)] have dips rather than peaks at the center, the leftward shift of the contributions from these Doppler groups cause the dip of Fig. 2(d) to shift left. Figure 4(a) shows the integrated contribution to the ac Stark shift for all Doppler groups from $-|\Delta f_D|$ to $|\Delta f_D|$ (assuming a Gaussian distribution of Doppler groups with $\Delta f_D^{\rm HWHM} = 80$ MHz). From the figure, one can see that the net ac Stark shift [from all Doppler groups, as can be read from the values at the right side of Fig. 4(a)] is negative, with positive shifts for low Δf_D, and larger negative shifts for intermediate Δf_D. The curves of Fig. 4(a) approach their final values already

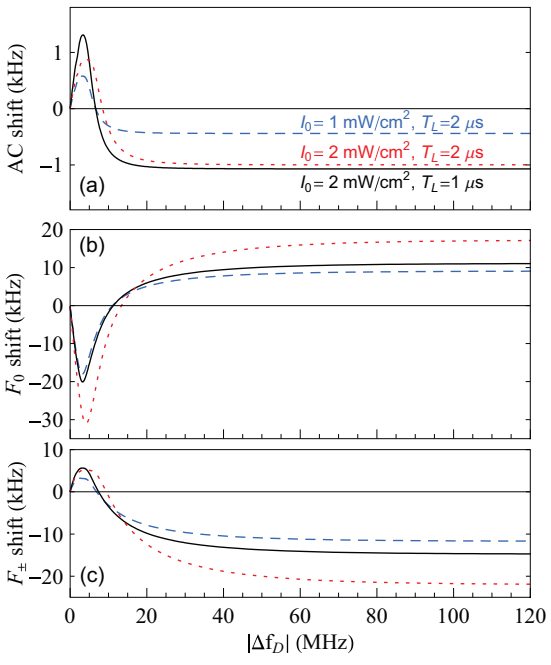

FIG. 4. (Color online) The ac Stark shifts (a) and interference shifts (b) and (c) of the $2\,^3S_1$-to-$2\,^3P_1$ saturated fluorescence dips. The graphs show integrated shifts due to Doppler groups ranging from $-|\Delta f_D|$ to $|\Delta f_D|$ and show that the shifts change sign for larger Doppler groups. Here a Gaussian distribution of Doppler groups with $\Delta f_D^{\rm HWHM} = 80$ MHz is assumed. The shifts are shown for three choices of intensity (I_0) and interaction time (T_L), as labeled in (a). The total shift (from all Doppler groups) is the value at the right of each curve.

TABLE I. ac Stark shifts and interference shifts for F_0 and $F_{\pm1}$ fluorescence. The shifts are in kHz and are for a selection of interaction times T_L and laser electric-field amplitudes E_0, and assume a Doppler profile with $\Delta f_D^{\rm HWHM} = 80$ MHz.

E_0	T_L	$2\,^3S_1$-to-$2\,^3P_0$			$2\,^3S_1$-to-$2\,^3P_1$		
(V/cm)	(μs)	ac	F_0	$F_{\pm1}$	ac	F_0	$F_{\pm1}$
0.375	0.25	0.09	0.03	−0.08	0.62	0.26	−1.16
0.375	0.5	0.03	0.08	−0.10	0.21	0.47	−1.48
0.375	1	0.01	0.11	−0.13	0.07	0.67	−2.07
0.375	1.5	0.00	0.15	−0.16	0.01	0.89	−2.49
0.375	2	0.00	0.18	−0.18	−0.01	1.15	−2.89
0.375	4	−0.01	0.35	−0.28	−0.06	2.38	−4.47
0.75	0.25	0.05	0.14	−0.14	0.21	1.12	−2.23
0.75	0.5	−0.01	0.28	−0.24	−0.17	2.45	−4.51
0.75	1	−0.02	0.48	−0.37	−0.26	3.74	−6.37
0.75	1.5	-0.03	0.65	−0.47	−0.30	4.95	−7.80
0.75	2	−0.03	0.83	−0.56	−0.31	6.22	−9.23
0.75	4	−0.03	1.51	−0.94	−0.33	11.3	−14.8
1.5	0.25	−0.25	0.98	−0.67	−3.41	12.8	−17.0
1.5	0.5	−0.17	1.48	−0.94	−2.04	13.4	−17.0
1.5	1	−0.15	2.06	−1.25	−1.72	17.0	−21.1
1.5	1.5	−0.15	2.64	−1.55	−1.63	21.2	−25.3
1.5	2	−0.14	3.22	−1.85	−1.56	25.5	−29.8
1.5	4	−0.14	5.48	−3.01	−1.50	42.7	−47.1
2.25	0.25	−0.54	2.87	−1.68	−3.91	19.5	−21.7
2.25	0.5	−0.47	3.36	−1.88	−5.31	30.7	−33.4
2.25	1	−0.38	4.43	−2.42	−4.18	37.4	−40.4
2.25	1.5	−0.35	5.56	−2.99	−3.82	45.8	−48.5
2.25	2	−0.34	6.72	−3.57	−3.65	54.6	−56.8
2.25	4	−0.33	11.2	−5.70	−3.46	89.8	−88.3
3	0.25	−0.68	3.30	−1.71	−11.0	40.0	−38.6
3	0.5	−0.86	5.79	−2.97	−9.79	53.7	−52.8
3	1	−0.68	7.44	−3.80	−7.60	64.6	−63.5
3	1.5	−0.63	9.29	−4.70	−6.89	78.3	−75.9
3	2	−0.61	11.2	−5.58	−6.57	92.8	−88.5
3	4	−0.59	18.6	−8.77	−6.21	152	−136

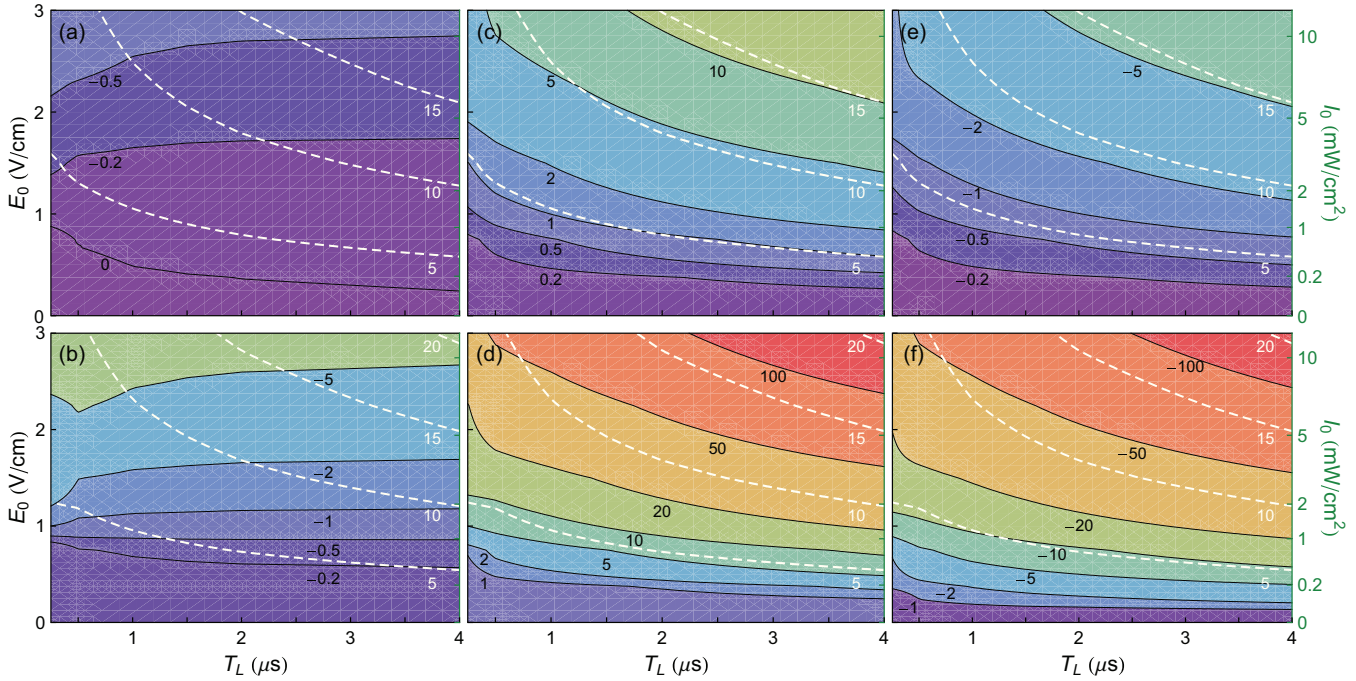

FIG. 5. (Color online) Contour graphs for ac Stark shifts and interference shifts vs interaction times T_L and laser intensities I_0. The shifts shown in (a), (c), and (e) are for the $2\,^3S_1$-to-$2\,^3P_0$ transition, and those in (b), (d), and (f) are for $2\,^3S_1$-to-$2\,^3P_1$. Plots (a) and (b) are ac Stark shifts. Plots (c) and (d) are interference shifts (which are to be added to the ac Stark shift) for $\Delta m_J = 0$ decays [F_0 in Eq. (8)], and (e) and (f) are interference shifts for $F_{\pm 1}$. A Doppler profile with $\Delta f_D^{\rm HWHM} = 80$ MHz is used. The shift values given along the black contour lines are in kHz. Also shown on the plots (white dashed lines) are the widths of the saturated fluorescence dips in MHz.

at $\Delta f_D \sim 30$ MHz, since the contributions from the larger Doppler groups [Fig. 2(c)] are well separated in frequency from the saturated fluorescence dip.

The shifts are determined from the frequencies of the half-maximum points [see Fig. 2(e)] for the line shapes obtained from the numerical integrations. Shifts for a range of interaction times T_L and intensities I_0 are shown in Table I and in Figs. 5(a) and 5(b). The ac Stark shifts are identical for F_{-1}, F_0, and F_{+1}. Note that the net shifts depend mostly on I_0, as would be naively expected for ac Stark shifts, but the graphs show dependence on T_L as well. These ac Stark shifts are small compared to the interference shifts discussed in the next section.

IV. INTERFERENCE SHIFTS

The interference shifts are the main focus of the current work. These shifts are obtained using the same methods as the ac Stark shifts described in the previous section. The saturated fluorescence line shapes are calculated by numerically integrating Eq. (5), including the off-diagonal $\gamma_{\mu jm}^{\mu' j' m'}$ terms. To determine the line shapes it is again necessary to do an integral over the time during which the atom passes through the laser beams, to perform an average over $\Delta\phi$ (the relative phase between the two laser beams), and to average over all of the Doppler groups Δf_D in the atomic beam. Figures 4(b) and 4(c) show that again the sign of the shift changes between small and larger values of $|\Delta f_D|$. As with the ac Stark shift, the interference shifts are determined from the frequencies of the calculated half-maximum points of the saturated fluorescence dips.

The results of the calculations (for a Doppler profile with $\Delta f_D^{\rm HWHM} = 80$ MHz) are shown in Table I and Fig. 5. The interference shifts in both the table and the figure are in addition to the ac Stark shifts discussed in the previous section. The table gives precise values for the shifts at certain values of T_L and I_0, and the figure gives contour graphs of the shifts. The contour graphs show that the interference shifts depend strongly on both T_L and I_0. For an actual experiment, the shift for different atoms in the beam would differ since I_0 depends on which part of the Gaussian laser beam the atom intersects, and T_L depends on the axial speed of the atom.

Table II shows shifts for other Doppler profiles. From this table it can be seen that the interference shift also depends on which Doppler groups are present in the beam, as would be expected from the dependence on Δf_D shown in Figs. 4(b) and 4(c). The table shows that the interference shifts for a beam with a Doppler width $\Delta f_D^{\rm HWHM} = 110$ MHz are approximately 50% larger than those for $\Delta f_D^{\rm HWHM} = 30$ MHz.

The interference shift results from a quantum-mechanical interference between the amplitude for obtaining fluorescence via an on-resonance laser excitation and the much smaller amplitude for obtaining fluorescence via a far-off-resonance excitation to a distant resonance. For example, the shift in the $2\,^3S_1(m = 0)$-to-$2\,^3P_0(m = 0)$ transition (the dashed arrow in Fig. 1) is due to the far-off-resonance $2\,^3S_1(m = 0)$-to-$2\,^3P_2(m = 0)$ transition. The far-off-resonance transition is 31.9 GHz away (20 000 natural widths), but still shifts the saturated fluorescence line shape at a level that is relevant for

TABLE II. The dependence of ac Stark shifts and interference shifts on the width ($\Delta f_D^{\mathrm{HWHM}}$) of the Doppler profile of the beam. Shifts of the $2\,^3S_1$-to-$2\,^3P_1$ saturated fluorescence dip, along with the FWHM and amplitude A [of Fig. 2(e)], are given for two laser intensities I_0 and two interaction times T_L.

I_0	T_L	$\Delta f_D^{\mathrm{HWHM}}$	Shifts (kHz)			FWHM	
($\mathrm{mW/cm^2}$)	(μs)	(MHz)	ac	F_0	$F_{\pm1}$	(MHz)	A
1	1	30	−0.45	3.8	−6.1	4.00	0.032
1	1	45	−0.43	4.5	−7.1	4.33	0.024
1	1	60	−0.42	4.9	−7.7	4.52	0.019
1	1	80	−0.41	5.2	−8.2	4.68	0.015
1	1	110	−0.41	5.6	−8.7	4.82	0.011
2	1	30	−1.10	8.2	−10.6	5.05	0.041
2	1	45	−1.09	9.5	−12.5	5.57	0.032
2	1	60	−1.08	10.4	−13.8	5.89	0.026
2	1	80	−1.07	11.3	−15.1	6.16	0.020
2	1	110	−1.06	12.0	−16.2	6.40	0.016
1	2	30	−0.48	6.4	−8.6	4.93	0.054
1	2	45	−0.47	7.4	−10.1	5.34	0.040
1	2	60	−0.46	8.0	−11.0	5.59	0.032
1	2	80	−0.45	8.5	−11.9	5.79	0.025
1	2	110	−0.44	9.0	−12.7	5.97	0.019
2	2	30	−1.04	13.0	−14.6	6.36	0.067
2	2	45	−1.03	14.8	−17.5	7.02	0.053
2	2	60	−1.02	16.1	−19.5	7.42	0.043
2	2	80	−1.01	17.3	−21.4	7.76	0.035
2	2	110	−1.00	18.4	−23.2	8.08	0.027

precision spectroscopy. The F_0 shifts are positive, while the $F_{\pm1}$ shifts are negative. The sign difference results from the opposite signs of γ_{000}^{020} and $\gamma_{\pm100}^{\pm120}$. The first of these (γ_{000}^{020}) is used in the interference for $2\,^3S_1(m=0)$ atoms which are laser excited to both the on-resonant $2\,^3P_0(m=0)$ state and the far-off-resonant $2\,^3P_2(m=0)$ state, followed by a decay from these states back down to the $2\,^3S_1(m=0)$ state with the emission of F_0 fluorescence. The second ($\gamma_{\pm100}^{\pm120}$) is used in the interference for $2\,^3S_1(m=0)$ atoms which are also laser excited to both the on-resonant $2\,^3P_0(m=0)$ state and the far-off-resonant $2\,^3P_2(m=0)$ state, but decay down to the $2\,^3S_1(m=\pm1)$ state with the emission of $F_{\pm1}$ fluorescence. For a typical saturated fluorescence measurement, where the width of the saturated fluorescence dip is approximately 10 MHz (as, for example, in Refs. [10,11]), shifts of between 3 and 6 kHz can be seen in Figs. 5(c) and 5(e).

Whether an experiment is subject to a positive or negative shift depends on whether it is sensitive to F_0 or $F_{\pm1}$ fluorescence, or to both. For example, if the fluorescence detector is placed above the laser beam (in the $\hat{z}$ direction), it is sensitive only to $F_{\pm1}$ fluorescence since the angular distribution of F_0 fluorescence is zero in this direction. In general, the shift is some linear combination of the shifts of Fig. 5(c) and of Fig. 5(e), with the linear combination determined by the geometry of the experiment and the polarization sensitivity of the detectors.

The shifts for the $2\,^3S_1$-to-$2\,^3P_1$ transition (the dotted arrows in Fig. 1) are much larger, since for this case the neighboring resonance (the $2\,^3S_1$-to-$2\,^3P_2$ transition) is 1400 natural widths away. These shifts are shown in Figs. 5(d) and 5(f) for F_0 and $F_{\pm1}$ fluorescence. Shifts of between 30 and 60 kHz for 10-MHz-wide saturated fluorescence dips can be seen on the contour graphs. These shifts are very large compared to the kHz or sub-kHz uncertainties of recent measurements [4–6,8,10,17–19] of the intervals. As before, F_0 and $F_{\pm1}$ show opposite shifts, so again the actual shift seen by a saturated fluorescence experiment depends on the geometry of the fluorescence detector. Although some cancellation can be expected between the positive and negative shifts for most detector geometries, the scale of the expected shifts is still of the order of 10 kHz, and therefore must be considered very carefully for precision measurements of the intervals.

As is the case for other instances of interference shifts from distant neighboring resonances [1–3,7], the scale of the shifts is given by the resonance width times the ratio of the resonance width to the frequency separation between the observed resonance and its neighboring resonance. This scaling can be seen in Figs. 5(c)–5(f), where the resonance width contours have the same general shape as the interference shift contours.

V. CONCLUSIONS

A systematic effect due to interference from distant neighboring resonances is shown to give shifts of tens of kilohertz for measurements of the $2\,^3S_1$-to-$2\,^3P_J$ energy intervals using the method of saturated fluorescence spectroscopy. These interference shifts are larger than shifts obtained using other measurement techniques for which the power used is near or below the saturation intensity for the transitions [3,7].

The interference shifts depend strongly on experimental parameters, including the peak intensity of the laser, the laser beam waist, the distribution of velocities in the atomic beam, and the relative detection efficiency for F_0 and $F_{\pm1}$ fluorescence. The relative detection efficiency determines the sign of the shift, and is affected by the geometry of the detector (since F_0 and $F_{\pm1}$ fluorescence have different angular distributions) and by the detection efficiency for different polarizations of light. Since the predicted shifts are large, careful modeling would be necessary to predict the shift to <1 kHz accuracy. This modeling would require a full simulation of the line shape including both the ac-shift and interference effects discussed in this work. The full simulation would require a properly weighted average over line shapes (obtained from integration of the density-matrix equations presented here) for atoms that experience different values of T_L, I_0, and Δf_D. The value of T_L experienced by a particular atom depends on the laser waist and the speed of the atom, whereas the value of I_0 depends on the power and waist of the laser, as well as the trajectory of the atom through this beam. A full simulation would require detailed information (at the percent level of accuracy) about the speed distribution, cross-sectional profile, and angular distribution of the atomic beam, and the waist and power of the laser beam. Additionally, the relative sensitivity to F_0 and $F_{\pm1}$ fluorescence would need to be modeled to the percent level of accuracy, which would require understanding at this level of the relative detection efficiency for different polarizations and the relative detection efficiency for fluorescence emitted at different angles.

The precise determination of interference shifts will make the next generation of helium 2^3P measurements using saturated fluorescence a challenge to interpret. Even for other laser and microwave measurement techniques, where the interference shifts are smaller [3,7], the interference shifts will have to be carefully considered in the program of determining the fine-structure constant from measurements of the 2^3P intervals. Similar analyses will have to be performed for other precise saturated fluorescence measurements, as well as for precision measurements using other techniques. This systematic shift has been overlooked in precision measurements, which sometimes determine line centers with uncertainties that are 1000–10 000 times smaller than the observed linewidth, where the effect could be significant even if the nearest-neighboring resonance is 1000–10 000 linewidths away from the resonance being measured.

ACKNOWLEDGMENTS

This work is supported by NSERC, CRC, ORF, CFI, and NIST, and computations were done using SHARCNET.

[1] M. Horbatsch and E. A. Hessels, Phys. Rev. A **82**, 052519 (2010).
[2] M. Horbatsch and E. A. Hessels, Phys. Rev. A **84**, 032508 (2011).
[3] A. Marsman, M. Horbatsch, and E. A. Hessels, Phys. Rev. A **86**, 012510 (2012).
[4] C. H. Storry, M. C. George, and E. A. Hessels, Phys. Rev. Lett. **84**, 3274 (2000).
[5] M. C. George, L. D. Lombardi, and E. A. Hessels, Phys. Rev. Lett. **87**, 173002 (2001).
[6] J. S. Borbely, M. C. George, L. D. Lombardi, M. Weel, D. W. Fitzakerley, and E. A. Hessels, Phys. Rev. A **79**, 060503 (2009).
[7] A. Marsman, M. Horbatsch, and E. A. Hessels, Phys. Rev. A **86**, 040501 (2012).
[8] J. Castillega, D. Livingston, A. Sanders, and D. Shiner, Phys. Rev. Lett. **84**, 4321 (2000).
[9] C. J. Sansonetti, C. E. Simien, J. D. Gillaspy, J. N. Tan, S. M. Brewer, R. C. Brown, S. Wu, and J. V. Porto, Phys. Rev. Lett. **107**, 023001 (2011); **109**, 259901(E) (2012); R. C. Brown, S. J. Wu, J. V. Porto, C. J. Sansonetti, C. E. Simien, S. M. Brewer, J. N. Tan, and J. D. Gillaspy, Phys. Rev. A **87**, 032504 (2013).
[10] F. Minardi, G. Bianchini, P. C. Pastor, G. Giusfredi, F. S. Pavone, and M. Inguscio, Phys. Rev. Lett. **82**, 1112 (1999); P. C. Pastor, G. Giusfredi, P. De Natale, G. Hagel, C. de Mauro, and M. Inguscio, *ibid.* **92**, 023001 (2004); G. Giusfredi, P. C. Pastor, P. De Natale, D. Mazzotti, C. de Mauro, L. Fallani, G. Hagel, V. Krachmalnicoff, and M. Inguscio, Can. J. Phys. **83**, 301 (2005).
[11] P. Cancio Pastor, L. Consolino, G. Giusfredi, P. De Natale, M. Inguscio, V. A. Yerokhin, and K. Pachucki, Phys. Rev. Lett. **108**, 143001 (2012).
[12] C. Y. She and J. R. Yu, Appl. Opt. **34**, 1063 (1995).
[13] C. Schwartz, Phys. Rev. **134**, A1181 (1964).
[14] Z.-C. Yan and G. W. F. Drake, Phys. Rev. Lett. **74**, 4791 (1995); T. Zhang, Z.-C. Yan, and G. W. F. Drake, *ibid.* **77**, 1715 (1996); G. W. F. Drake, Can. J. Phys. **80**, 1195 (2002).
[15] K. Pachucki and J. Sapirstein, J. Phys. B **33**, 5297 (2000); **36**, 803 (2003); K. Pachucki, Phys. Rev. Lett. **97**, 013002 (2006).
[16] K. Pachucki and V. A. Yerokhin, Phys. Rev. Lett. **104**, 070403 (2010).
[17] D. Shiner, R. Dixson, and P. Zhao, Phys. Rev. Lett. **72**, 1802 (1994); D. L. Shiner and R. Dixson, IEEE Trans. Instrum. Meas. **44**, 518 (1995); M. Smiciklas and D. Shiner, Phys. Rev. Lett. **105**, 123001 (2010).
[18] T. Zelevinsky, D. Farkas, and G. Gabrielse, Phys. Rev. Lett. **95**, 203001 (2005).
[19] C. H. Storry and E. A. Hessels, Phys. Rev. A **58**, R8 (1998).
[20] D. A. Cardimona, M. G. Raymer, and C. R. Stroud, Jr., J. Phys. B **15**, 55 (1982); D. A. Cardimona and C. R. Stroud, Phys. Rev. A **27**, 2456 (1983).